Effects of optically shallow bottoms on upwelling radiances: Inhomogeneous and sloping bottoms

Curtis D. Mobley[1] *and Lydia K. Sundman*

Sequoia Scientific, Incorporated, Westpark Technical Center, 15317 Northeast 90th Street, Redmond, Washington 98052

Abstract

If the benthic boundary in optically shallow waters is spatially inhomogeneous or sloping, the underwater light field is inherently three-dimensional (3D). Numerical simulations of 3D underwater radiances were made for environmental conditions observed in shallow Bahamian waters. The simulations show that if the pattern of bottom reflectance for an inhomogeneous but level bottom has a spatial scale much smaller than the bottom area seen by a radiometer, the inhomogeneous bottom can be replaced by a homogeneous bottom whose reflectance is the area-weighted average of the actual bottom reflectances. For large-scale patterns of bottom reflectance, the 3D light fields near the edges of bottom patches of different reflectances can be predicted from analytical models incorporating the sensor geometry and one-dimensional (1D) light fields computed for homogeneous bottoms, with errors of order 10% when compared to the exact 3D solutions. The same holds true for uniformly sloping bottoms, whose 3D light fields can be modeled in terms of the 1D light fields computed for level bottoms, with errors of less than 10% for bottom slopes of 20° or less.

Optically shallow bottoms affect the reflected, upwelling radiance in various ways. Mobley et al. (2003) investigated how the bidirectional reflectance distribution function (BDRF) of a level homogeneous bottom determines the magnitude and angular distribution of the bottom-reflected radiance. If the bottom is inhomogeneous, or patchy, the upwelling radiance is a spatial function of horizontal location as well as depth; the same is true if the bottom is not level. This paper considers the effects of patchy and sloping bottoms on the upwelling radiances.

One-dimensional (1D) radiative transfer models like Hydrolight (Mobley et al. 1993; Mobley 1994) are computationally extremely fast. However, to achieve their mathematical efficiency, such models require that the water inherent optical properties (IOPs, namely the absorption coefficient and the volume scattering function) and the boundary conditions (the sea surface wave statistics and the bottom BRDF) be horizontally homogeneous. Thus, the computed in-water light field can vary spatially with depth, but not with horizontal location. If the bottom BRDF varies with position, or if the bottom is not level, then the assumption of a horizontally homogeneous bottom boundary condition is violated and 1D models cannot be used. In these cases, the inherently three-dimensional (3D) light field generated by horizontal variations in the bottom boundary condition can be computed by Monte Carlo techniques.

Consider, for example, a level bottom with a large seagrass patch next to a large sand patch. In principle, the entire light field is then 3D. However, near the center of the seagrass patch, far from its boundary with the sand, a 1D model that assumes an infinitely large, homogeneous patch of seagrass may be able to predict the light field with sufficient accuracy for the problem at hand. Likewise, near the center of the sand patch, the light field may be essentially 1D. Near the grass–sand boundary, the light field will show effects of both bottom types, and a 3D model must be used for exact computation of the light field. However, the computer times required for 3D Monte Carlo calculations are vastly greater than for 1D Hydrolight calculations, both because of the different numerical techniques used to solve the radiative transfer equation and because of the additional calculations required for 3D versus 1D geometries. It is therefore of interest to quantify when bottom-induced 3D effects on the upwelling radiance are large enough to warrant the computational expense of Monte Carlo techniques, and when the 3D light field can be adequately approximated by a 1D light field. Near the grass–sand boundary just mentioned, it may even be possible to approximate the true 3D light field by some combination of the 1D grass and sand solutions. If this is indeed the case, the computational savings would be considerable. Likewise, if the bottom is not level, 3D Monte Carlo techniques must be used. However, it may be possible to approximate the true 3D light field at a given horizontal location by a 1D light field computed using the depth at that location, after some correction for the bottom-slope effect is applied to the 1D solution. This paper investigates the errors in such 1D approximations to 3D light fields.

The BMC3D model

To compute 3D light fields, we developed a backward Monte Carlo (BMC) 3D computer code (named BMC3D) capable of simulating in-water light fields for various inhomogeneous bottom conditions. Collins et al. (1972) and Gordon (1985) describe the mathematical details of the BMC computational technique. In brief, as illustrated in Fig. 1, the BMC technique emits simulated photon packets from the
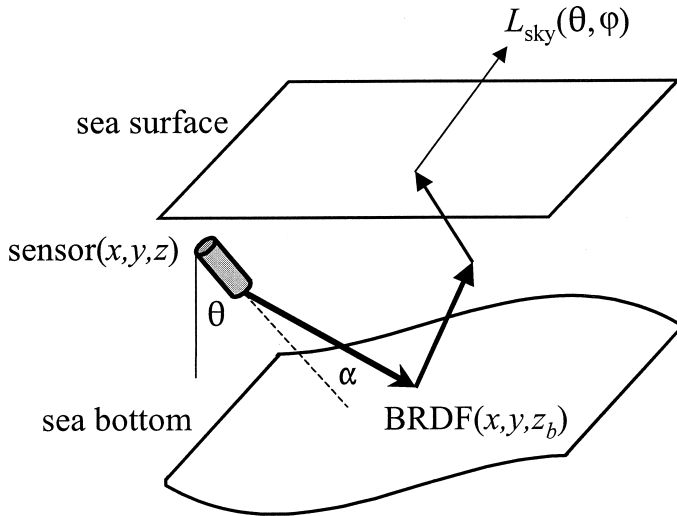

Fig. 1. Illustration of backward Monte Carlo ray tracing. The photon packets are traced from the sensor to the sky, rather than from the sky to the sensor.

sensor in an angular pattern determined by the radiometric quantity being computed—radiance, plane, or scalar irradiance. The photon packets are then traced using standard Monte Carlo techniques (e.g., Mobley et al. 1993; Mobley 1994) as the photon packets interact with the water body, the bottom, and the sea surface. Whenever a photon packet strikes the bottom, the BRDF at that location is used as a bivariate probability distribution function to determine the polar and azimuthal directions and the weight of the reflected photon packet. Thus any bottom geometry or reflectance pattern can be incorporated into the BMC3D code by defining the bottom depth as a function of horizontal location and the BRDF to be used at each bottom point. Whenever a photon packet exits the sea surface heading toward the sky, it is weighted by the sky radiance in that direction and tallied as a contribution to the power received by the in-water sensor. This is equivalent to tracing a photon packet traveling in the opposite direction from the sky to the sensor. One advantage of the BMC artifice is that only photon packets connecting the sky and the sensor are traced. No photon packets miss the sensor, as would be the case in a forward computation in which photon packets are traced from the sky into the water, of which only a few eventually would enter the sensor at a particular location and orientation. The BMC3D calculations thus have no wasted photons and the code is consequently very efficient for a Monte Carlo simulation. Another advantage of the BMC technique is that it can simulate point sensors and radiances as measured by an idealized sensor having a Dirac delta-function angular response. Neither point sensors nor delta-function responses can be simulated with forward Monte Carlo techniques. The BMC3D code does not employ any variance reduction techniques.

The BMC3D code uses a Cartesian (x, y, z) coordinate system to locate the sensor and specify the bottom boundary. Here x and y are horizontal coordinates lying in the plane of the mean sea surface and oriented as appropriate for the problem at hand. The depth z is measured positive downward from the mean sea surface; the bottom depth at hori-

zontal position (x, y) is then $z = z_b(x, y)$. For example, $x \leq 0$ might be a half plane with a bottom covered by seagrass, and $x > 0$ might be a half plane with a sandy bottom. The origin of the coordinates would then be at the sea surface directly above the grass–sand boundary. The sensor can be placed at any (x, y, z) position within the water, and it can be oriented in any direction (θ, φ), where θ is measured from the $+z$ (nadir) direction and φ is measured from the $+x$ direction. Thus, a radiance sensor pointing in the $\theta = 0$ direction is collecting photons heading in the $\theta = 180°$ direction; i.e., it is measuring the upwelling radiance L_u. The sensor angular response is specified by polar angle α and azimuthal angle β. Angle $\alpha = 0$ along the sensor's optical axis, i.e., $\alpha = 0$ in the sensor viewing direction (θ, φ); β is measured from some convenient direction. In BMC simulations, a delta-function sensor response is then simulated by emitting all photons with $\alpha = 0$. Most sensors have responses that are symmetric about their optical axis, in which case β is randomly chosen from a uniform distribution over 0 to 2π. A cosine response (as used in measuring the plane irradiance) is simulated by emitting the photons in randomly chosen directions (α, β), with α being determined from a probability distribution that reproduces the cosine response (namely, $\alpha = \sin^{-1} \sqrt{\mathfrak{R}}$, where $\mathfrak{R}$ is a random number drawn from a uniform 0 to 1 distribution). A measured sensor response $S(\alpha)$ can be used to determine the distribution of photons as a function of α appropriate to any actual sensor.

Our interest here is on bottom effects. The simulations below therefore assume the water body itself to be homogeneous, i.e., the IOPs are independent of depth and horizontal location. When a photon packet crosses the mean sea surface, a tilted wave facet is randomly generated using Cox–Munk wave slope statistics (Cox and Munk 1954; *see* Mobley 1994 for computational details), which reproduce the slope statistics of actual gravity-capillary wave sea surfaces for the given wind speed. This tilted wave facet is used to compute the directions and weights of the reflected and refracted photon packets according to Fresnel's law and the angle of incidence of the photon packet onto the tilted wave facet. The possibility of multiple scattering between surface wave facets is ignored. The close agreement of BMC3D and Hydrolight (which does include multiple interactions between surface wave facets) for comparable situations indicates that the error associated with ignoring multiple scattering between surface wave facets is negligible for solar positions and viewing directions away from the horizon (when wave shadowing may be important). The sky radiance distribution for given atmospheric conditions is determined using a combination of the Radiance Transmittance RAD-TRAN atmospheric model (Gregg and Carder 1990) for the spectral plane irradiance and the Harrison and Coombes (1988) semianalytical model for the directional pattern of the sky radiance relative to the sun's location; these same models are used in Hydrolight for computing sky radiances.

Mobley et al. (2003) showed that for sand and various vegetation canopies a non-Lambertian bottom BRDF can be replaced by a Lambertian BRDF having the same irradiance reflectance R_b, and the resulting errors in the upwelling radiances will be no more than 10% for solar angles and view-

ing directions relevant to much ocean-color remote sensing or in-water observation of the bottom using ambient light. To simplify the BMC3D calculations, we therefore assume the bottom to be a Lambertian reflector at each point, although the bottom reflectance R_b can depend on horizontal location and wavelength. (The BMC3D code can simulate non-Lambertian bottoms, but at considerable computational expense if the BRDF is not a simple analytical function.) The bottom need not be level in the BMC3D code. For non-level bottoms, the Lambertian BRDF is applied to the tangent plane to the bottom at the point where the photon packet intersects the bottom.

The BMC3D code was debugged using a combination of hand checking, comparison with Hydrolight for comparable simulations using homogeneous bottoms (e.g., the points at $x = \pm\infty$ in Figs. 2 and 4 below), and comparison with idealized situations (e.g., no absorption or no scattering) for which analytic solutions of the radiance could be obtained.

Environmental conditions

Our intention in this paper is to illustrate 3D bottom effects on upwelling light fields for environmental conditions relevant to remote sensing in clear, optically shallow waters; we do not perform an exhaustive study for all water types. For the simulations below, we therefore selected water IOPs and bottom conditions typical of those measured near Lee Stocking Island, Bahamas during the Coastal Benthic Optical Properties (CoBOP) field experiments in 1999 and 2000. These waters are visually quite clear with underwater visibilities of 10 m or more. The total (water plus dissolved substances plus particles) absorption coefficients are at a minimum at blue wavelengths. In one instance (channel marker site 1, 24 May 1999) the total absorption coefficient at 480 nm, as obtained from ac-9 measurements, was $a = 0.05$ m^{-1} and the scattering coefficient was $b = 0.28$ m^{-1}. These values give a beam attenuation coefficient of $c = a + b = 0.33$ m^{-1}; one optical depth, $1/c$, is then 3 m. The corresponding albedo of single scattering is $\omega_0 = b/c = 0.85$, which indicates scattering-dominated water. The total IOPs as measured at 658 nm were $a = 0.40$ and $b = 0.20$, for which $\omega_0 = b/c = 0.33$, which indicates absorption-dominated water. The scattering phase function was not measured; we therefore use the average particle phase function defined in Mobley et al. (1993). The contribution by sea water to the total scattering at 480 nm is only 0.0034 m^{-1}, which justifies the use of a particle phase function for the total phase function. The wind speed was taken to be 5 m s^{-1}, and the sky was clear.

A bottom reflectance of $R_b = 0.05$ at 480 nm is typical of seagrass leaves measured at the CoBOP site and of various algae (Maritorena et al. 1994). The visually bright ooid sands at the CoBOP site typically have a reflectance near $R_b = 0.5$ at 480 nm. We use these values to simulate the extremes encountered in bottom reflectances.

Small-scale patch effects

We first consider the effects of variations in the bottom reflectance that are of a much smaller spatial scale than the

bottom area "seen" by the sensor. Such a situation would occur, for example, if seagrass leaves were viewed against a sand substrate by a radiance sensor whose field of view included many individual leaves.

To simulate this situation, the bottom was modeled as a checkerboard pattern of two different reflectances. The checkerboard squares were given a size of 0.01 m on a side. To represent 25% grass coverage seen against a sand substrate, for example, 25% of the checkerboard squares were given a reflectance of $R_b = 0.05$ and the remaining squares were given the sand reflectance $R_b = 0.5$. A radiance sensor with a 5° half angle field of view located at the surface in 5 m of water would see a circle of radius (5 m) $\times$ tan 5° = 0.44 m on the bottom. (This sensor response was chosen for comparison with Hydrolight, which has a 5° half angle polar cap.) This sensor footprint would include about 6,000 individual squares. Simulations of this type with the BMC3D code show that the radiance computed for the checkerboard bottom with two different reflectances differs less than 1% from the radiance computed for a uniform bottom having the same area-weighted reflectance. Thus the 25% grass, 75% sand bottom just mentioned can be replaced by a uniform bottom having a reflectance of $R_b = 0.25 \times 0.05 + 0.75 \times 0.5 = 0.3875$. In the present situation, the Hydrolight results agreed with the uniform-bottom BMC3D results to within 1%, which represents statistical fluctuations in the BMC3D estimates.

These results indicate that in simulations of bottoms with small-scale variability compared to the sensor footprint, a 1D model like Hydrolight can be used with an area-weighted bottom reflectance determined from the actual bottom reflectances. The more expensive 3D simulation is unnecessary.

Large-scale patch effects

If the bottom patches are large compared to the sensor footprint, we can anticipate "edge effects" near the boundaries of the large patches. We thus investigated the 3D light field near the edge of semiinfinite bottom patches of greatly different reflectances. The BMC3D coordinate system was chosen with the x axis perpendicular to the boundary between the two bottom types and the y axis lying along the boundary. Bottom type 1, $x \leq 0$, has the grass reflectance $R_b = 0.05$; bottom type 2, $x > 0$, has the sand reflectance $R_b = 0.5$. The bottom was level at a depth of $z_b = 5$ m (1.65 optical depths at 480 nm). The sun was placed at a zenith angle of 60° in air in the $+x$ ($\varphi = 0$) direction.

In the first simulation, BMC3D was used to compute the upwelling plane irradiance just below the sea surface, $E_u(x, z = 0)$, as the sensor is moved across the grass–sand boundary. The diamonds in Fig. 2 show the irradiances as computed by one series of BMC3D runs. The cluster of diamonds plotted at $x = 0$ shows the results from 10 independent runs (each starting with a different seed for the random number generator). The spread of these points gives a qualitative indication of the magnitude of the statistical noise in the BMC3D estimates of $E_u(x, z = 0)$. The dashed lines at $E_u = 0.036$ and 0.167 W m^{-2} nm^{-1} show the irra-
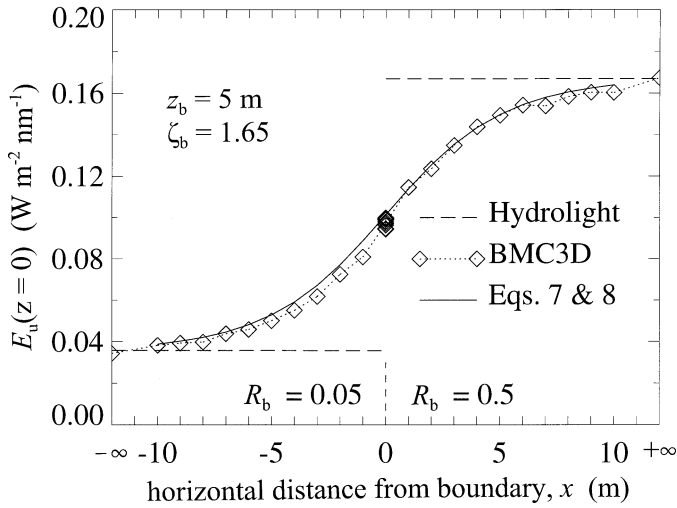
Fig. 2. Simulations of the upwelling plane irradiance just below the sea surface across a grass–sand boundary at $x = 0$. Line type and symbols identify the model used.

Fig. 3. Contribution of bottom-reflected light to the upwelling irradiance and radiance just below the sea surface, as computed by Eq. 1: (a) E_u for highly scattering water ($\omega_0 = 0.85$); (b) E_u for highly absorbing water ($\omega_0 = 0.33$); (c) L_u for highly scattering water; (d) L_u for highly absorbing water. The solid lines are for a zenith sun, and the dashed lines are for a solar zenith angle of 60° in air. The upper pair of lines in each panel is for a bottom reflectance of $R_b = 0.05$, and the bottom pair is for $R_b = 0.50$. The dots in panel a correspond to the simulation of Fig. 2.

diances computed by Hydrolight for homogeneous bottoms with reflectances of 0.05 and 0.5, respectively. The points labeled $x = \pm\infty$ are the BMC3D values obtained for simulations of infinite homogeneous bottoms. These values agree with Hydrolight to within a few percent; the difference can be attributed to statistical noise in the Monte Carlo simulations. The BMC3D values show a transition zone between the grass and sand bottoms that extends horizontally about twice the water depth. At distances from the grass–sand boundary greater than ~10 m, the sensor is primarily influenced by only one bottom type and the 1D solution provides an approximation to the exact 3D solution that is accurate to within 10% or better.

Each BMC3D-computed point in Fig. 2 required about 20 min of computer time (on a 600 MHZ PC) when 10^6 photons were initialized. A corresponding Hydrolight run for a homogeneous bottom requires only 3 s and gives the entire radiance distribution at all depths, not just the surface upwelling irradiance being studied here. Thus there is great computational incentive to model the 3D light field in the transition region near the grass–sand boundary in terms of the respective 1D Hydrolight solutions, which are valid far from the boundary.

To lay the foundation for such a simplified model, we next investigate how much of the upwelling irradiance or radiance at the water surface is due to light that has reflected off of the bottom itself and how much is due to light that has been scattered upward within the water column, without ever having interacted with the bottom. A series of Hydrolight runs was performed for a totally absorbing (black) bottom defined by $R_b = 0$, for a dark bottom (like dense seagrass) with $R_b = 0.05$, and for a highly reflecting bottom (like ooid sand) with $R_b = 0.50$. A measure of the contribution of the bottom-reflected light to the upwelling irradiance at the sea surface, $E_u(z = 0)$, is the ratio

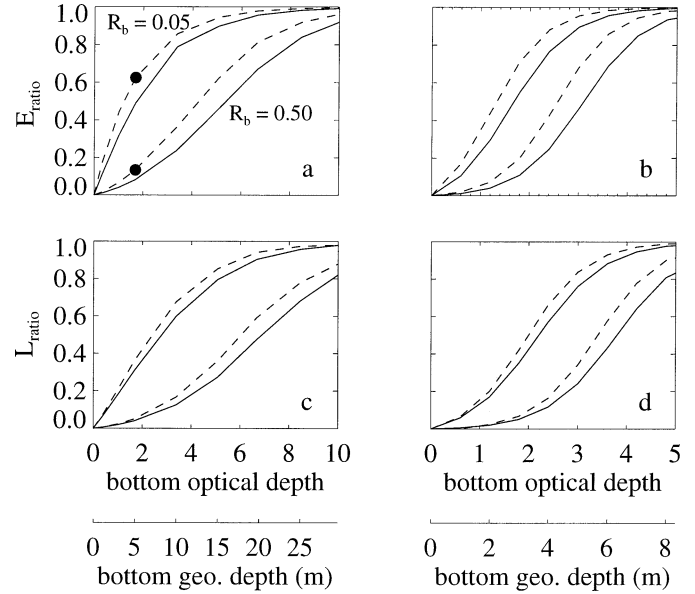$$E_{\text{ratio}} = \frac{E_u(R_b = 0)}{E_u(R_b > 0)} \qquad (1)$$

If this ratio is zero, the water column is contributing nothing to the upwelling irradiance; this is the limit as the bottom depth goes to zero. If this ratio is one, the bottom is contributing nothing; this occurs as the bottom depth becomes infinite. A similar ratio can be defined for the upwelling radiance L_u.

Figure 3 shows these ratios as functions of bottom depth and reflectance for solar zenith angles (in air) of 0 (solid lines) and 60° (dashed lines), and for highly scattering ($\omega_0 = 0.85$; panels a and c) and highly absorbing ($\omega_0 = 0.33$; panels b and d) water IOPs. The conversion from optical depth $\zeta = cz$ to geometric depth z in meters is based on the IOPs at 480 and 658 nm, as described above. The two dots in panel a correspond to the 5-m bottom depth and 60° solar angle used to generate Fig. 2. This figure shows that for bright bottoms at less than a few optical depths, most of the upwelling light at the surface has interacted with the bottom. The water column has a greater contribution to the upwelling light for the 60° solar zenith angle than for the sun at the zenith simply because the solar direct beam path within the water is longer for a given bottom depth. These simulations do not separate the contributions of photons that travel directly from the bottom to the sensor from the contributions of bottom-reflected photons that have been scattered again within the water column. However, the highly forward peaked nature of the scattering phase function implies that the majority of photons travel almost directly from the bottom to the sensor when the bottom depth is no more than a few photon mean free paths $1/c$ (3 m at 480 nm and 1.67 m at

658 nm in the present simulations); this is the case for the shallow bottom depths of interest here. For a given bottom optical depth and reflectance, the bottom contribution is less for highly absorbing waters than for highly scattering waters.

We now construct an analytical model for the upwelling irradiance $E_u(x, z = 0)$, as was computed for Fig. 2. The upwelling plane irradiance just below the sea surface is by definition

$$E_u(x, y, z = 0) = \int_{\Xi_u} L_u(x, y, z = 0, \theta, \varphi)|\cos \theta|\, d\Omega \quad (2)$$

where L_u is the upwelling radiance. Ξ_u is the set of all upward directions, $\pi/2 \le \theta \le \pi$ and $0 \le \varphi \le 2\pi$; and $d\Omega = \sin\theta\, d\theta\, d\varphi$ is the differential element of solid angle. As just discussed, in optically shallow waters the upwelling radiance will be dominated by bottom-reflected radiance that travels almost directly from the bottom to the sensor. We thus assume that we can ignore the path radiance contribution to L_u, i.e., we ignore the scattering by the water column itself of the solar beam into the sensor. The radiance at the surface, $L_u(x, y, 0, \theta, \varphi)$, then arises from the upward-reflected radiance at the bottom, $z = z_b$, attenuated along the path from the bottom to the surface:

$$L_u(x, y, 0, \theta, \varphi) = L_u(x', y', z'_b, \theta, \varphi)\exp(-cz'_b/|\cos \theta|) \quad (3)$$

Here (x', y', z'_b) is the point on the bottom where radiance reflected into direction (θ, φ) reaches the surface at location $(x, y, 0)$. Substituting Eq. 3 into Eq. 2, we can rewrite the integral as a sum of integrals over the two bottom types:

$$E_u(x, y, z = 0)$$
$$= \int_{\Xi(1)} L_u(x', y', z'_b, \theta, \varphi)\exp(-cz'_b/|\cos \theta|)|\cos \theta|\, d\Omega$$
$$+ \int_{\Xi(2)} \cdots \quad (4)$$

Here $\Xi(1)$ is the set of (θ, φ) directions that ''sees'' bottom type 1 from point $(x, y, 0)$, and $\Xi(2)$ is the set of directions that sees bottom type 2. The integral over $\Xi(2)$ has the same form as the integral over $\Xi(1)$. The set of all upward directions is $\Xi_u = \Xi(1) + \Xi(2)$.

For a Lambertian bottom, the upwelling radiance at the bottom is related to the upwelling and downwelling irradiances by

$$L_u(x', y', z'_b, \theta, \varphi) = E_u(x', y', z'_b)/\pi = R_b(x', y', z'_b)E_d/\pi$$

Hydrolight simulations show that the bottom boundary reflectance R_b seldom perturbs the downwelling irradiance by more than a few percent, even for optically very shallow waters. For example, in the extreme cases of $R_b = 0.05$ versus 0.50 at a depth of 1 m in water with the highly scattering IOPs described above, E_d at the bottom varies by only 9% about the mean value, although the two E_u values differ by an order of magnitude; for deeper waters the variation is less (e.g., E_d at the bottom varies by less than 4% when the bottom depth is 5 m). Thus, it is reasonable to assume that the bottom type does not perturb the downwelling irradiance,

in which case the upwelling irradiance at the bottom will depend on the bottom type via the bottom reflectance R_b, but not on the location within a bottom patch of a given type. The upwelling irradiance then can be replaced by the upwelling irradiance computed by a 1D model for the bottom reflectance of the particular bottom type. Equation 4 can then be written as

$$E_u(x, y, z = 0)$$
$$= \frac{E_u(1; z_b)}{\pi} \int_{\Xi(1)} \exp(-cz_b/|\cos \theta|)|\cos \theta|\, d\Omega$$
$$+ \frac{E_u(2; z_b)}{\pi} \int_{\Xi(2)} \exp(-cz_b/|\cos \theta|)|\cos \theta|\, d\Omega \quad (5)$$

Here arguments 1 and 2 have been added to the irradiances to indicate that these values are computed by a 1D model for bottom types 1 or 2. To the same level of approximation as Eq. 4, the 1D irradiances at the surface can be written in terms of the irradiances at the bottom, e.g.,

$$E_u(1; z = 0)$$
$$= E_u(1; z_b) \int_{\Xi} \frac{1}{\pi}\exp(-cz_b/|\cos \theta|)|\cos \theta|\, d\Omega \quad (6)$$

with a corresponding equation for bottom type 2.

Finally, we note that the $\cos \theta$ factor in Eq. 2 is just the angular response function $S(\alpha)$ for a plane irradiance sensor: $\alpha = \theta$ for a sensor whose optical axis is oriented downward. This factor can be replaced by any other sensor response $S(\theta)$ to describe other radiometric variables. With this generalization, and using Eq. 6 to write $E_u(i; z_b)$ in terms of $E_u(i; 0)$, $i = 1$ or 2, Eq. 5 becomes

$$E_u(x, y, 0) = E_u(1; 0)w(1; x, y) + E_u(2; 0)w(2; x, y) \quad (7)$$

where $w(i; x, y)$ is the weighting function for bottom type i, which in general is given by

$$w(i; x, y) = \frac{\displaystyle\int_{\Xi(i)} \exp[-cz_b/|\cos \theta|]S(\theta)\, d\Omega}{\displaystyle\int_{\Xi} \exp[-cz_b/|\cos \theta|]S(\theta)\, d\Omega} \quad (8)$$

For the plane irradiances of Eq. 7, the sensor response function in Eq. 8 is $S(\theta) = \cos \theta$. Equation 7 can be generalized to any number of bottom types; note that $\Sigma_i\, w(i; x, y) = 1$.

Equations 7 and 8 give a conceptually simple analytical model for the 3D upwelling irradiance at any horizontal location (x, y) in terms of the 1D irradiances computed for homogeneous bottoms of the various types, and in terms of weighting functions that depend only on the water beam attenuation coefficient c and the viewing geometry of the various bottom patches as seen from location (x, y). The weighting functions generally need to be computed numerically, but evaluation of these integrals is much faster than performing 3D Monte Carlo simulations. The adequacy of the assumptions leading to this model of course depends on the water IOPs and bottom depth and reflectance of each specific situation.
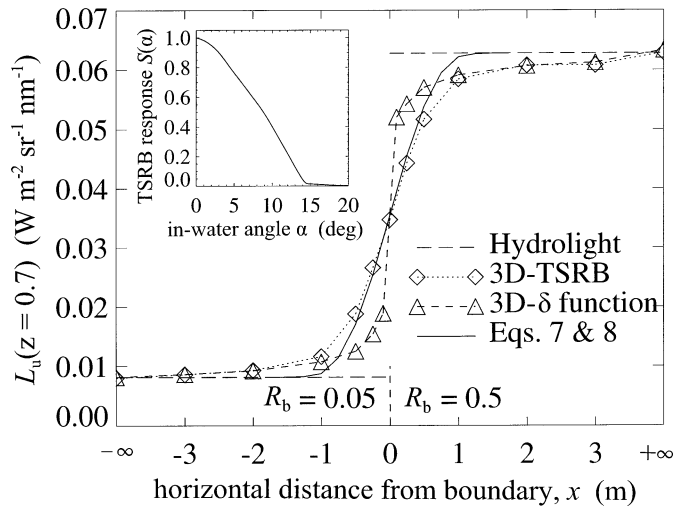
Fig. 4. Simulations of the upwelling radiance as measured by a TSRB across a grass–sand boundary at $x = 0$. Line type and symbols identify the model used. The inset shows the actual TSRB sensor response used in the BMC3D calculations for the TSRB curve.

The solid line in Fig. 2 shows $E_u(x, 0)$ as predicted by Eqs. 7 and 8. The 1D irradiances $E_u(1; 0)$ and $E_u(2; 0)$ were computed by Hydrolight using the bottom reflectances of $R_b(1) = 0.05$ and $R_b(2) = 0.5$, respectively. Near the grass–sand boundary, the 1D Hydrolight values differ from the 3D BMC3D values by up to $\pm 70\%$. The average of the 10 BMC3D runs plotted at $x = 0$ differs from the analytical model prediction by 3.6%. At the other points, the analytical model of Eqs. 7 and 8 is never more than 10% from the 3D values, and some (unknown) part of that difference is due to statistical noise in the BMC3D values, rather than to the inadequacy of the analytical model itself. Thus, for this particular set of water IOPs and bottom reflectances, the analytical model based on 1D calculations gives E_u to within 10% of the BMC3D values, but at a small fraction of the computational cost.

Figure 4 shows the predicted values for the upwelling radiance as would be measured by a tethered spectroradiometer buoy (TSRB; Satlantic) being towed across the same grass–sand boundary as was simulated in Fig. 2. The TSRB radiance sensor is at a nominal depth of 0.7 m below the sea surface. The TSRB sensor response $S(\alpha)$ is shown in the inset of Fig. 4. The sensor response drops to half of its peak value at an angle of $\alpha \approx 9°$ and is almost 0 beyond 14°. For this water depth, the grass–sand boundary does not come into the sensor field of view until the TSRB is closer than 4.3 tan (14°) ≈ 1.1 m from the boundary.

As in Fig. 2, the dashed lines show the Hydrolight values for $L_u(z = 0.7$ m) computed for the two different bottom reflectances. The diamond symbols show the L_u values as predicted by the BMC3D code using the measured TSRB angular response function. The triangle symbols show the L_u values as predicted by BMC3D using a Dirac delta function for the sensor response $S(\alpha)$, i.e., the simulated sensor has a perfectly collimated acceptance direction. Because the idealized delta-function sensor has a zero field of view, the

differences in the BMC3D and Hydrolight values, which are noticeable within ~ 3 m of the boundary, can be attributed to scattering effects within the water column. Scattering blurs the boundary between the two bottom types, so that when the sensor is above the grass, for example, it is detecting some photons that originated from downwelling light being reflected by the sand bottom and then being scattered again by the water into the sensor. Note that the curves for the actual TSRB sensor and the delta-function sensor are almost identical for distances greater than 1 m from the boundary, which indicates that the TSRB is receiving light scattered by the water column but that it is not directly seeing the adjacent bottom type. When the TSRB is closer than 1.1 m to the boundary, its finite field of view also collects light directly from both bottom types, which broadens the L_u transition from one bottom type to the other.

The analytical model of Eqs. 7 and 8 is applicable to the TSRB if the 1D E_u values of Eq. 7 are replaced by 1D values for $L_u(z = 0.7$ m), and the measured TSRB sensor response is used for $S(\theta)$ in Eq. 8. The resulting prediction for the 3D L_u is shown by the solid line in Fig. 4. We see that these values begin to depart from the Hydrolight values at ~ 1 m from the boundary, where the sensor begins seeing the adjacent bottom type in its field of view. The model values are identical with Hydrolight farther from the boundary because the model does not account for scattering within the water column, which causes additional blurring of the boundary in the BMC3D calculations. In this simulation, the analytical model differs from the BMC3D values by as much as 25% (near $x = -1$ m), but this is still better than the 1D Hydrolight values, which differ by $\pm 80\%$ near the boundary.

These simulations show that the errors resulting if a 1D radiative transfer model is used without correction to estimate the upwelling light field near the boundary between bottom types having much different reflectances can be many tens of percent, compared to the correct 3D values. However, the 3D edge effects can be analytically modeled using the 1D values in combination with weighting functions that incorporate water beam attenuation and sensor response effects. The resulting estimates of the upwelling light fields often have errors of less than 10%, and the computations take seconds rather than minutes or hours. These errors are proportionately less if the reflectances of the bottom patches are closer in value than the order-of-magnitude difference in R_b values used in these simulations.

Bottom-slope effects

We next consider the extent to which the 3D light field induced by a sloping bottom can be approximated by a 1D model. Figure 5 illustrates a radiance sensor at the sea surface viewing a sloping bottom. The bottom slopes downward in the $+x$ direction at an angle θ_b, measured from 0 for a level bottom. The bottom depth directly below the sensor is z_b. The sun's direct beam within the water has a zenith angle of θ_{sw} in the (x, y, z) coordinate system, which has x and y parallel to the mean sea surface. The incident angle of the sun's beam onto the bottom is θ_i, measured from the normal to the bottom. The sun's azimuthal angle is φ_s, measured from 0 in the $+x$ direction.
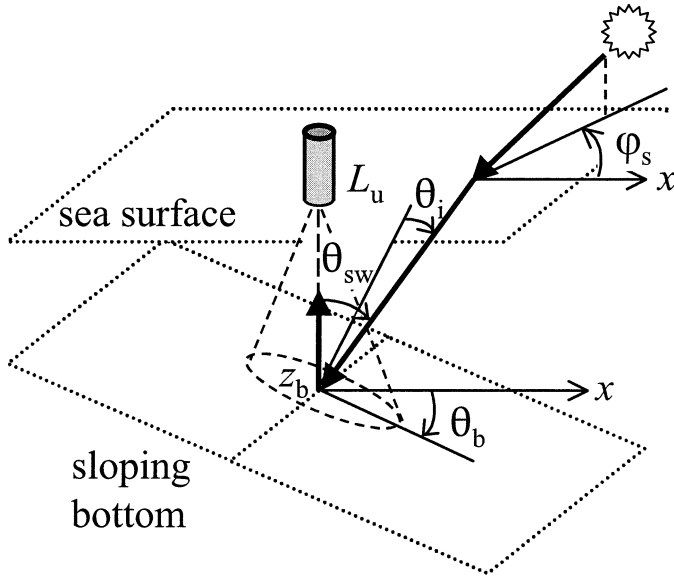
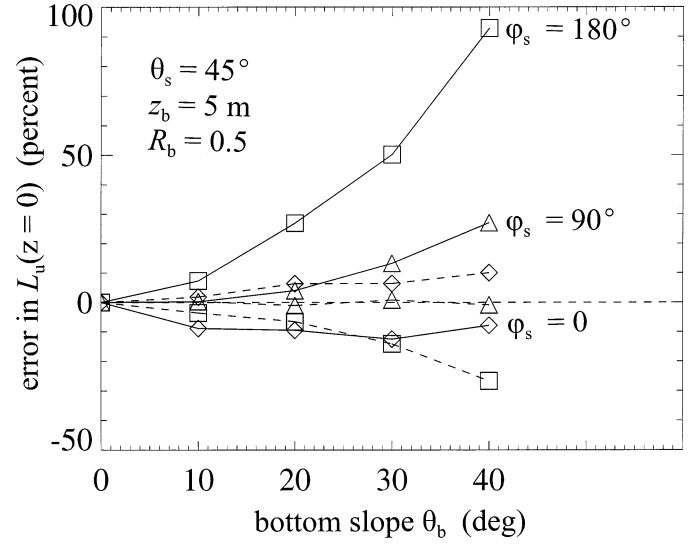Fig. 5.   Geometry for simulation of a sloping bottom.

Fig. 6.   Errors in the upwelling radiance that occur if a 1D model with a level bottom is used instead of a 3D model with a sloping bottom (solid lines). The azimuthal angle $\varphi_s = 0$ indicates the sun downslope, and $\varphi_s = 180$ indicates the sun upslope (*see* Fig. 5). The dashed lines are the errors obtained when the 1D, level-bottom radiances are corrected by the model of Eq. 9.

Using the same water IOPs at 480 nm as in the previous simulations, the upwelling radiance just below the sea surface, $L_u(z = 0)$, was computed for a variety of bottom-slope angles θ_b, solar zenith and azimuthal angles, and bottom depths and reflectances, using the BMC3D code. For comparison with Hydrolight, the radiance sensor was modeled with a 5° top-hat response, i.e., $S(\alpha) = 1$ for $0 \leq \alpha \leq 5°$, and $S(\alpha) = 0$ for $\alpha > 5°$. Hydrolight was used to compute L_u for the same conditions, except that the bottom had a constant depth equal to the depth directly below the sensor in the BMC3D simulations. The error in L_u, as computed by the 1D Hydrolight model compared to the 3D BMC3D model, was computed as

$$\text{percent error} = 100\frac{L_u(1D) - L_u(3D)}{L_u(3D)}$$

The solid lines of Fig. 6 show the results for a solar zenith angle of 45° in air, a bottom depth of 5 m directly below the sensor, and a bottom reflectance of $R_b = 0.5$. The error in L_u resulting from using a 1D model instead of a 3D model can be tens of percent or greater, especially when the sun is upslope ($\varphi_s = 180°$). This is the solar azimuthal angle that causes the greatest change in $\cos \theta_i$, compared to the $\cos \theta_i$ value for a level bottom.

In optically shallow waters with a Lambertian bottom BRDF, it is reasonable to assume that the primary effect of the bottom slope is that it changes the sun's incident angle onto the bottom. If this is indeed the case, then it should be possible to correct for the bottom slope by a simple adjustment for the change in incident angle. If $E_\perp$ is the irradiance of the sun's direct underwater beam measured on a surface normal to the beam, then the irradiance onto a surface oriented at angle θ_i is $E_\perp \cos \theta_i$. The ratio of the radiances reflected by a sloping Lambertian bottom to that of a level bottom is then

$$\frac{L_u^{\text{slope}}}{L_u^{\text{level}}} = \frac{\dfrac{R_b}{\pi}E_\perp \cos \theta_i^{\text{slope}}}{\dfrac{R_b}{\pi}E_\perp \cos \theta_i^{\text{level}}}$$

where superscripts slope and level denote values for sloping and level bottoms, respectively. Thus the 3D upwelling radiance for the sloping bottom can be estimated from the 1D value computed for a level bottom by the simple equation

$$L_u^{\text{slope}} = L_u^{\text{level}}\frac{\cos \theta_i^{\text{slope}}}{\cos \theta_i^{\text{level}}} \tag{9}$$

The angle of incidence onto the sloping bottom is given by

$$\cos \theta_i^{\text{slope}} = \sin \theta_b \sin \theta_{\text{sw}}\cos \varphi_s + \cos \theta_b \cos \theta_{\text{sw}} \tag{10}$$

where all angles are measured in water, i.e., θ_{sw} is the sun's zenith angle after refraction through the sea surface.

The dashed lines of Fig. 6 show the errors in L_u resulting when the 1D Hydrolight values for L_u^{level} are used in Eq. 9 to estimate the 3D L_u^{slope} values. For this simulation, the error is less than 15% for bottom slopes of 30° or less. The errors are greater for larger solar zenith angles, but even for zenith angles of 60° (in air), the modeled L_u values are within 7% of the BMC3D values for bottom slopes of 20° or less. Again, we see that if errors of order 10% are tolerable, it is possible to use a 1D radiative transfer model like Hydrolight in combination with a simple model for the bottom-slope effect to obtain an estimate of the true radiance, which can be exactly computed only by running a 3D radiative transfer code like BMC3D.

Conclusions

Numerical simulations of three-dimensional underwater light fields were made using a backward Monte Carlo model capable of simulating spatially patchy and sloping bottom boundaries. The results from the 3D Monte Carlo model were compared with results obtained from the 1D Hydrolight model. For level bottoms with patchiness spatial scales much smaller than the instrument footprint, the patchy bottom can be replaced by a uniform bottom whose reflectance is the area-weighted average of reflectances of the various bottom reflectances. A 1D radiative transfer model can then be used to compute the in-water and water-leaving radiance distribution. If the bottom patches are spatially large compared to the instrument footprint, the errors in upwelling radiances and irradiances can be many tens of percent if a 1D model is used near the boundary between bottom patches of different reflectances. However, the errors can be reduced to ~10% or less in many situations of practical interest if the 1D predictions, valid for homogeneous bottoms, are adjusted using simple analytical models that account for water attenuation and sensor response. The same is true for uniformly sloping bottoms, whose primary effect is to change the incident angle of the sun's direct beam onto the smooth bottom. A simple geometrical correction for the bottom slope, when applied to the 1D solution for a level bottom, can give upwelling radiances that are within 10% of the exact values computed by a 3D radiative transfer model for bottom slopes up to 20°. In these situations it is necessary to run a computationally expensive 3D Monte Carlo model only if upwelling radiances or irradiances must be computed with accuracies of 10% or better. Although our results, strictly speaking, are valid only for the particular water IOPs and other conditions used in the simulations, the corresponding results for other optically shallow, clear water bodies are likely to be similar.

References

COLLINS, D. G., W. G. BLÄTTNER, M. B. WELLS, AND H. G. HORAK. 1972. Backward Monte Carlo calculations of the polarization characteristics of the radiation emerging from spherical-shell atmospheres. Appl. Optics **11:** 2684–2696.

COX, C., AND W. MUNK. 1954. Measurement of the roughness of the sea surface from photographs of the sun's glitter. J. Opt. Soc. Am. **44:** 838–850.

GORDON, H. R. 1985. Ship perturbation of irradiance measurements at sea. 1: Monte Carlo simulations. Appl. Opt. **24:** 4172–4182.

GREGG, W. W., AND K. L. CARDER. 1990. A simple spectral solar irradiance model for cloudless maritime atmospheres. Limnol. Oceanogr. **35:** 1657–1675.

HARRISON, A. W., AND C. A. COOMBES. 1988. Angular distribution of clear sky short wavelength radiance. Solar Energy **40:** 57–63.

MARITORENA, S., A. MOREL, AND B. GENTILI. 1994. Diffuse reflectance of oceanic shallow waters: Influence of the water depth and bottom albedo. Limnol. Oceanogr. **39:** 1689–1703.

MOBLEY, C. D. 1994. Light and water: Radiative transfer in natural waters. Academic.

———, H. ZHANG, AND K. J. VOSS. 2003. Effects of optically shallow bottoms on upwelling radiances: Bidirectional reflectance distribution function effects. Limnol. Oceanogr. **48:** 337–345.

———, AND OTHERS. 1993. Comparison of numerical models for computing underwater light fields. Appl. Opt. **32:** 7484–7504.